

The effect of curvature and topology on membrane hydrodynamics

Mark L. Henle¹, R. McGorty^{3,4}, A. D. Dinsmore³, and Alex J. Levine^{1,2}

¹*Department of Chemistry and Biochemistry, University of California, Los Angeles, CA 90095*

²*California Nanosystems Institute, University of California, Los Angeles, CA 90095*

³*Department of Physics, University of Massachusetts, Amherst, Massachusetts 01003, USA*

⁴*Department of Physics, Harvard University, Cambridge, MA 02138*

(Dated: February 5, 2008)

We study the mobility of extended objects (rods) on a spherical liquid-liquid interface to show how this quantity is modified in a striking manner by both the curvature and the topology of the interface. We present theoretical calculations and experimental measurements of the interfacial fluid velocity field around a moving rod bound to the crowded interface of a water-in-oil droplet. By using different droplet sizes, membrane viscosities, and rod lengths, we show that the viscosity mismatch between the interior and exterior fluids leads to a suppression of the fluid flow on small droplets that cannot be captured by the flat interface predictions.

The dynamics of mobile inclusions in lipid membranes are fundamental to a variety of biological processes, including signal transduction [1] and the endocytosis of bacterial toxins [2]. Membrane inclusions, such as proteins [3] or lipid “rafts” [4], are in many cases significantly larger than the lipids making up the membrane, so their dynamics can be studied in terms of macroscopic objects moving in a continuum fluid environment. Additionally, elucidating the mobilities and hydrodynamic interactions of colloidal particles at a fluid–fluid interface has important technological ramifications for the design and formation of membranes and capsules composed of particles assembled on droplets [5].

Low Reynolds number hydrodynamics in viscous membranes or interfaces differs substantially from the better-known problem of hydrodynamics in three dimensions. Because of the coupling between the two-dimensional membrane and its surrounding viscous solvent, in-plane momentum in the membrane is lost to the surrounding fluid. The flows induced in the surrounding fluid generate nonlocal couplings between the membrane velocity and stress. The net result of these effects is to introduce an inherent length scale ℓ_0 – the Saffman-Delbrück (SD) length – which is set by the ratio of the (2D) membrane viscosity η_m to the (3D) fluid viscosity η , $\ell_0 \sim \eta_m/\eta$ [6]. For cellular plasma membranes $\ell_0 \simeq 1\mu\text{m}$ [7]. In contrast, low-Reynolds number hydrodynamics in 3D fluids is a scale-invariant theory. The existence of an inherent length scale in membrane and interfacial hydrodynamics has complex and rather subtle effects on a variety of problems, including protein diffusion in cell membranes [6, 8], the flow of monolayers through channels [9], the dynamics of monolayer domains [10], microrheology of fluid–fluid interfaces [11], and the mobilities of rigid and flexible extended objects in membranes [12].

In this letter we explore the effect of nontrivial interfacial geometry and topology on the hydrodynamics of viscous interfaces. We find two principal results with broad implications for particulate transport on curved or spherical interfaces. The first is that the compact topology of

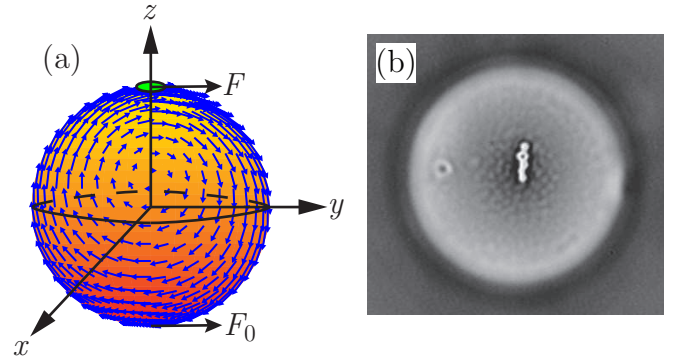


FIG. 1: (color online) (a) Schematic illustration and calculated membrane velocity field of a point particle of radius a (green disk) at the north pole subject to a force \mathbf{F} , with a pinning force \mathbf{F}_0 at the south pole. Here the interior and exterior fluids are identical: $\eta_+ = \eta_-$, $R/\ell_0 = 0.1$ and $R/a = 100$. (b) Image from a connected rod of paramagnetic PMMA colloids at the interface of a water-in-hexadecane droplet decorated with microparticles.

a spherical interface fundamentally alters the nature of the 2D interfacial velocity field. On a sphere, any vector field must include at least two vortices [13]. In contrast, there are no such singularities in the velocity field on an infinite, flat interface. Secondly, the curvature of the interface introduces a new length scale – the radius of curvature, R . This geometric length scale competes with ℓ_0 in determining the hydrodynamics of particles embedded in the interface. Thus, geometry plays a role in particulate transport on par with viscosity. These results have important biophysical implications, such as the retardation of the diffusive transport of membrane-bound proteins in highly curved regions of the membrane.

To develop a theory of the hydrodynamics of curved surfaces we ignore inertial effects and impose force balance at the interface. Specifically, we consider the response of an *incompressible* (i.e. constant area) spherical interface of radius R and its surrounding fluids to a tangential point force $\mathbf{F} = F\hat{y}$ applied at the north pole

of the interface, as illustrated in Fig. 1(a). Because of the curvature of the interface, the in-plane force balance equation must be written in a manifestly covariant form:

$$f_{\alpha}^{\text{ext}} = \eta_m g^{\beta\gamma} [D_{\gamma} D_{\beta} v_{\alpha} + D_{\gamma} D_{\alpha} v_{\beta}] - \sigma_{\alpha r}^{-} + \sigma_{\alpha r}^{+}, \quad (1)$$

where $g^{\beta\gamma}$ is the contravariant metric tensor and D_{α} is the covariant derivative; the Greek indices run over the polar and azimuthal angles θ, ϕ , respectively. $\mathbf{f}^{\text{ext}} = F\delta(\theta)\hat{\mathbf{y}}/(2\pi R^2)$ is the external force density applied at the north pole. The term in brackets in Eq. (1) is the viscous force density resulting from gradients in the interfacial velocity field v_{α} ; the last two terms are the viscous stresses due to solvent inside (σ^{-}) and outside (σ^{+}) the spherical surface, $\sigma_{ij}^{\pm} = \eta_{\pm} [D_i v_j^{\pm} + D_j v_i^{\pm}] - P_{\pm} \delta_{ij}$, where P_{\pm} , η_{\pm} , and \mathbf{v}^{\pm} are the hydrostatic pressures, viscosities, and velocities, respectively, of the solvents inside (−) and outside (+) the sphere. To determine the solvent stresses on the interface, we must solve the incompressible Stokes equation inside and outside the sphere using the “stick” boundary conditions $\mathbf{v}^{\pm}|_{r=R} = \mathbf{v}$.

It is convenient to decompose the dynamical system into normal modes consisting of the combined flows of the interface and the interior and exterior solvents. The deformations of a 2D interface can be decomposed into bending, compression, and shear modes. However, the incompressibility of the interface prevents compression and, when combined with the incompressibility of the interior fluid, bending modes of the interface. The remaining shear modes can be written in terms of the (manifestly covariant) curl of a scalar field, $v_{\alpha} = \epsilon_{\alpha\beta} D^{\beta} \Psi$, where $\epsilon_{\alpha\beta}$ is the alternating tensor. The combined interface and solvent system is diagonalizable in a basis of spherical harmonics [14, 15]. In the region exterior to the sphere, we retain only those terms that vanish at infinity. This eliminates the solution that corresponds to the uniform center of mass translation of the sphere with respect to the surrounding fluid.

By expanding the delta functions in \mathbf{f}^{ext} in spherical harmonics and applying the in-plane force balance condition Eq. (1), we determine the amplitude of each normal mode of the combined interface/solvent system generated by the external force. The interfacial velocity is then given by

$$\mathbf{v} \cdot \hat{\theta} = -V \sin \phi \sum_{l=1}^{l_{\max}} \frac{1}{s_l} \csc \theta P_l^1(\cos \theta), \quad (2)$$

$$\mathbf{v} \cdot \hat{\phi} = -V \cos \phi \sum_{l=1}^{l_{\max}} \frac{1}{s_l} [\cot \theta P_l^1(\cos \theta) + P_l^2(\cos \theta)], \quad (3)$$

where $V = F/(4\pi\eta_m)$, $P_l^m(x)$ is the l -th associated Legendre function, and

$$s_l = \frac{l(l+1)}{2l+1} \left[l(l+1) - 2 + \frac{R}{\ell_-} (l-1) + \frac{R}{\ell_+} (l+2) \right]. \quad (4)$$

The upper limit on the sums is defined below.

In Eq. (4) we have defined two lengths in analogy to the SD length: $\ell_{\pm} = \eta_m/\eta_{\pm}$. For the case of a flat interface between two differing fluids, these two lengths enter symmetrically, so that the only one length scale controls the interfacial hydrodynamics: $\ell_0 = \eta_m/(\eta_- + \eta_+)$. Here the two lengths enter independently.

The most striking manifestation of the effect of the interior/exterior solvent asymmetry occurs in the limit of a large interior viscosity, $\eta_+ \gg \eta_-$. This causes the $l=1$ term in Eq. (4) to dominate the sums in Eqs. (2) and (3). As a result, the external force at the north pole causes a rigid rotation of the interface and interior fluid. The opposite limit $\eta_+ \gg \eta_-$ will *not* have an analogous effect. However, for a small enough sphere, $R \ll \ell_+$, the same rigid body rotation is observed. Thus, geometry alone can have a dramatic effect on interfacial hydrodynamics.

In order to prevent the rigid rotation of the sphere, we apply a pinning force \mathbf{F}_0 at the south pole that forces the total fluid velocity to vanish at the point (see Fig. 1a). Because of the linearity of the Stokes equation, the total response of the fluids and interfaces is simply the sum of the individual responses to each force. A typical solution for the interfacial velocity field on the sphere is shown in Fig. 1a. The appearance of a vortex in the upper hemisphere is required by topological constraints; there is a similar one placed symmetrically on the back side of the sphere (not shown).

The particle’s mobility μ , defined by $\mathbf{v} = \mu \mathbf{F}$, is given by [see Eqs. (2) and (3)]

$$\mu = \frac{1}{4\pi\eta_m} \sum_{l=1}^{l_{\max}} \frac{l(l+1)}{2s_l}. \quad (5)$$

The finite particle radius a sets the upper limit $l_{\max} = 8R/9a$ of the sums in Eqs. (2), (3), and (5). It is determined by the requirement that the Stokes mobility for a sphere of radius a is recovered for the case $\eta_+ = \eta_-$ with a vanishing interfacial viscosity ($\eta_m \rightarrow 0$) [11].

In Fig. 2 we plot the dimensionless mobility $\eta_m \mu$ for a particle at the north pole of a pinned spherical membrane as a function of R for a variety of interior viscosities η_- . In all cases, the flat-interface SD result $\eta_m \mu_{\text{SD}} \approx \ln(\ell_0/a)/4\pi$ (horizontal dashed lines) is recovered in the limit $R \rightarrow \infty$. However, when $R/\ell_+ \ll 1$, $\eta_m \mu \rightarrow \ln(R/a)/2\pi$ (dot-dashed line). Hence, particle mobilities in high-curvature membranes, $R/\ell_0 \ll 1$, are depressed relative to the SD result (this regime is not shown for the green/gray curve in Fig. 2). For intermediate curvatures, the mobility on a sphere can be enhanced or suppressed relative to the SD result, depending on the value of the ratio η_+/η_- . For $\eta_+/\eta_- < 1$ (green/gray curve), the mobility in a spherical membrane is larger than the flat membrane mobility because the more viscous fluid is bounded inside the spherical membrane; consequently, it dissipates less energy than in the case where

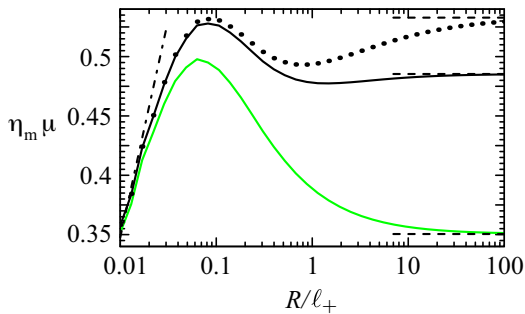


FIG. 2: (color online) Dimensionless mobility $\eta_m \mu$ for a particle at the north pole of a pinned spherical membrane as a function of the membrane radius R , for $\ell_+ = 10\mu\text{m}$, $a = 0.01\mu\text{m}$, and $\eta_- = 10\eta_+$ (green/gray curve), $\eta_- = \eta_+$ (black curve), or $\eta_- = 0.1\eta_+$ (dotted curve). The dashed and dot-dashed lines indicate the theoretical asymptotic results (see text).

its domain is unbounded. Conversely, when $\eta_+/\eta_- > 1$ (dotted curve), the mobility in a spherical membrane is *suppressed* relative to the flat membrane case.

To calculate the mobility of extended objects, we use the superposition principle applicable to this linear system [16]. Specifically, we consider a rod of length L embedded in the membrane. We approximate the rod by $N + 1$ disks of radius a separated by a distance b , where $L = Nb + 2a$. We also apply a pinning force at the south pole that sets the fluid velocity to zero at that point; this force mimics the adsorption of the droplet on the substrate in our experiments [17]. Using the superposition principle, the total interfacial velocity $v_\alpha^{\text{tot}}(\theta, \phi) = \sum_{i=0}^{N+1} \mathbf{F}_\beta^{(i)} \chi_{\alpha,\beta}(\theta, \phi; \theta_i, \phi_i)$. Here, $\mathbf{F}^{(i)}$ is the force applied to the disk at the point (θ_i, ϕ_i) ; $i = 0$ corresponds to the south pole, and $i = 1, \dots, N + 1$ labels the disks in the rod. We consider only forces parallel to the rod axis. The response function $\chi_{\alpha,\beta}(\mathbf{x}; \mathbf{y})$ gives $v_\alpha^{\text{tot}}(\mathbf{x})$ due to a unit force in the β direction applied at \mathbf{y} .

To determine the forces $\mathbf{F}^{(i)}$, we require that the total fluid velocity vanishes at the south pole, and that each disk in the rod move with unit velocity. These constraints provide a set of $N + 2$ linear equations that determine $\mathbf{F}^{(i)}$. Summing the $N + 1$ forces acting on the rod moving at unit velocity gives the inverse mobility of the rod. Using this same set of forces we can also calculate the entire velocity field in response to the rod's motion, both on the sphere and in the surrounding fluids.

We performed experiments to measure the flow fields on spherical droplets coated with a monolayer of small (370 nm) sterically-stabilized polymethylmethacrylate (PMMA) particles [18]. Water droplets ($\eta_- = 10^{-3}$ N s/m²), typically 30-100 μm in diameter, suspended in hexadecane ($\eta_+ = 3.34 \times 10^{-3}$ N s/m²) provided the spherical interface. The PMMA particles served dual roles: to set the interfacial viscosity and to allow the flow field to be measured using video microscopy and particle-tracking software. To create the flow field, we

added micron-sized paramagnetic polystyrene particles (carboxylate-functionalized, DVB-crosslinked, 0.95 μm in diameter; item #MC04N, lot 3251 from Bangs Laboratories). These paramagnetic spheres also adsorbed at the interface. In the presence of a magnetic field, they formed a single rod-like aggregate on the droplet. This rod was then moved along the surface of the droplet by a permanent magnet brought close to the sample.

Samples were observed under bright-field microscopy using a Zeiss Axiovert 200. Images were captured at 30 frames/second and analyzed with particle tracking code written in IDL [19]. The PMMA beads were first tracked without any magnetic field gradient present, and their mean squared displacements were used to determine the interfacial viscosity η_m . To measure the flow field, $\approx 10^2$ PMMA particles were tracked while a single chain on the interface was moved at speeds of approximately a few $\mu\text{m/s}$. For each droplet, the process was repeated twelve times, and the mean and statistical uncertainty of the flow velocities was measured. Droplets of different radii, chain lengths, and viscosities were used.

In Fig. 3 we plot (points) the measured interfacial velocity, $\mathbf{v}_{\text{exp}} = v_{\text{exp}}(x)\hat{\mathbf{y}}$, along the line that perpendicularly bisects the rod (i.e. the line $\phi = 0, \pi$, $0 < \theta < \pi$), as a function of the distance $x = R \sin \theta$ from the north pole in the $\hat{\mathbf{x}}$ -direction. We also show the predictions of the flat interface theory (FIT, dashed lines) [12] and spherical interface theory (SIT, solid lines); each curve is obtained by direct calculation using no adjustable parameters. We account for the rod thickness in the theory by setting $v_{\text{exp}} = v_0$ everywhere within the rod. In Figs. 3(a) – Fig. 3(c), we show a sequences of droplets demonstrating the increasing effect of curvature. In Fig. 3(a), where $R \gg \ell_0$, we see that both the FIT and SIT agree with the data. In Fig. 3(b), where $R \gg \ell_0$, but is now comparable to L , the effects of curvature begin to be seen. However, only when ℓ_0 approaches R , as in Fig. 3(c), does the effect of curvature become dramatic. Here the velocity field decays significantly more rapidly than FIT predictions. This is primarily because of the viscosity mismatch between the less viscous interior (water) and more exterior (oil) fluids, which leads to a relative decrease in the particle mobilities on the spherical interface (dotted curve in Fig. 2). In this case the SIT prediction is a significant improvement over that of the FIT.

This work demonstrates the considerable effect of interfacial curvature and topology on the transport of particles embedded in the interface. The topology of the sphere requires the formation of vortices in steady-state, zero Reynolds number flow, and the ratio of the radius of curvature of the interface to the SD length characterizing its 2D hydrodynamics determines the location of these vortices relative to the moving particle. These effects have direct implications for the kinetics of particulate aggregates on the surface of droplets. In the future we will consider related problems on cylindrical

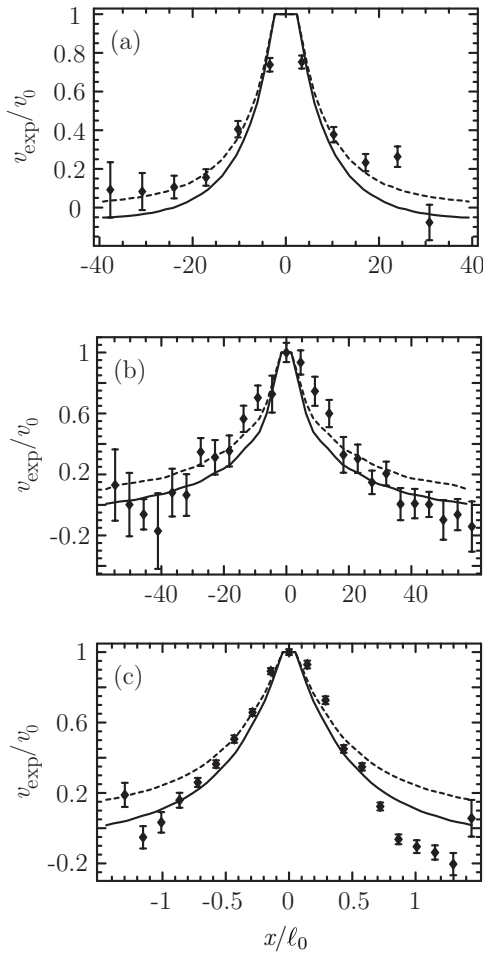


FIG. 3: Experimental data (points) and theoretical predictions (solid curves) for the interfacial velocity v_{exp} measured along the perpendicular bisector of the rod and normalized by the velocity v_0 of the rod. The dashed line shows the corresponding predictions for rod's velocity field on a flat interface [12]. The theoretical curves were generated using the parameters: (a) $\ell_0 = 0.2\mu\text{m}$, $L = 6.4\mu\text{m}$, $R = 17.5\mu\text{m}$, $N = 30$. This data corresponds to Fig 1(b); (b) $\ell_0 = 0.3\mu\text{m}$, $L = 31.6\mu\text{m}$, $R = 54\mu\text{m}$, $N = 35$; (c) $\ell_0 = 9.5\mu\text{m}$, $L = 7\mu\text{m}$, $R = 26\mu\text{m}$, $N = 10$.

membranes, where we can separate the effects of curvature and topology. We have also demonstrated that a viscosity mismatch between the interior and exterior solvents can lead to either significant increases or decreases in the diffusivity of interface-bound particles depending on sphere radius. These effects may play an important role in protein transport on membranes separating the viscous cytosol [20] from extracellular fluids.

AJL thanks T. Liverpool for enjoyable and enlightening discussions. MLH and AJL were supported in part by NASA NRA 02-OBPR-03-C. ADD acknowledges support through a Faculty Research Grant from the University of Massachusetts, Amherst. ADD and RM thank A. B. Schofield for the PMMA spheres and Kan Du and the

microscopy facilities of the NSF-funded UMass Materials Research Science and Engineering Center on Polymers for technical assistance.

-
- [1] J. Schlessinger, *Cell* **110**, 669 (2002); S. M. Dunham *et al.*, *J. Phys. Chem. B* **108**, 10540 (2004).
 - [2] L. Abrami *et al.*, *J. Cell. Biol.*, **160**, 321 (2003).
 - [3] E. A. J. Reits and J. J. Neefjes, *Nat. Cell Biol.* **3**, E145 (2001).
 - [4] F.R. Maxfield and I. Tabas, *Nature* **438**, 612 (2005).
 - [5] A. D. Dinsmore *et al.*, *Science* **298**, 1006 (2002); Y. Lin *et al.*, *Langmuir* **21**, 191 (2005); C. Zeng, H. Bissig, and A.D. Dinsmore, *Sol. State Comm.*, **139**, 547 (2006); L. Zheng and S. Granick, *Nanolett.*, **6**, 694 (2006).
 - [6] P. G. Saffman and M. Delbruck, *Proc. Natl. Acad. Sci.* **72**, 3111 (1975); H.A. Stone and A. Ajdari *J. Fluid Mech.* **369**, 151 (1998). See also H.A. Stone, *J. Fluid Mech.* **409**, 165 (2000).
 - [7] F. Pinaud, Ph.D. Thesis. UCLA (2007).
 - [8] B.D. Hughes, B.A. Pailthorpe, and L.R. White, *J. Fluid Mech.* **110**, 349 (1981).
 - [9] D.K. Schwartz, C.M. Knobler, and R. Bruinsma, *Phys. Rev. Lett.* **73**, 2841 (1994); H.A. Stone *Phys. Fluids* **7**, 2931 (1995).
 - [10] H.A. Stone and H.M. McConnell, *Proc. R. Soc. London Ser. A* **448**, 97 (1995); H.A. Stone and H.M. McConnell, *J. Phys. Chem.* **99**, 13505 (1995); D.K. Lubensky and R.E. Goldstein, *Phys. Fluids* **8**, 843 (1996).
 - [11] A. J. Levine and F. C. MacKintosh, *Phys. Rev. E* **66**, 061606 (2002); V. Prasad, S.A. Koehler, and E.R. Weeks, *Phys. Rev. Lett.* **97**, 176001 (2006); A. Anguelouch, R.L. Leheny, and D.H. Reich, *Appl. Phys. Lett.* **89**, 111914 (2006).
 - [12] A. J. Levine, T. B. Liverpool, and F. C. MacKintosh, *Phys. Rev. E* **69**, 021503 (2004); A. J. Levine, T. B. Liverpool, and F. C. MacKintosh, *Phys. Rev. Lett.* **93**, 038102 (2004).
 - [13] John Milnor, *Topology from the Differentiable Viewpoint*, Princeton Landmarks in Mathematics, (Princeton University Press, Princeton) 1965.
 - [14] J. Happel and H. Brenner, *Low Reynolds number hydrodynamics* (Kluwer, 1983, Boston).
 - [15] M. L. Henle and A. J. Levine, *to be published*.
 - [16] J.G. Kirkwood and J. Riseman, *J. Chem. Phys.* **16**, 565 (1948).
 - [17] Aside from pinning of the fluid velocity at the point of contact, we do not account for the hydrodynamic interaction between the sphere and the substrate.
 - [18] P. Pieranski, *Phys. Rev. Lett.* **45**, 569 (1980).
 - [19] J.C. Crocker and D.G. Grier, *J. Colloid Interf. Sci.* **179**, 298 (1996).
 - [20] Y.C. Fung, *Biomechanics: Mechanical Properties of Living Tissues, Second Edition*, Springer-Verlag, New York, 1993